An investigation of the wake recovery of two model horizontal-axis tidal stream turbines measured in a laboratory flume with particle image velocimetry

Stephen M. Simmons[a] s.simmons@hull.ac.uk

Stuart J. McLelland[a] s.j.mclelland@hull.ac.uk

Daniel R. Parsons[a] d.parsons@hull.ac.uk

Laura-Beth Jordan[a] L.Jordan@2013.hull.ac.uk

Brendan J. Murphy[a] b.j.murphy@hull.ac.uk

Lada Murdoch[b] lada@cfdpeople.com

[a]*School of Environmental Sciences, University of Hull, Cottingham Road, Hull, HU6 7RX, UK*

[b]*CFD People Ltd., North Lanarkshire, UK*

Corresponding author: Stephen Simmons, s.simmons@hull.ac.uk

ABSTRACT: The uptake of tidal stream-turbine (TST) technology lags other renewable energy sources despite the advantages of predictability, stability and increased power output in comparison to wind turbines of the same dimensions. There remains a need to address environmental concerns about the potential impacts of TSTs including the suspension and deposition of bed sediments if TSTs are to be more widely accepted and deployed. Sediment mobilisation and persistent flow vortices will also adversely affect the performance of other TST devices in an array downstream of the wake. The focus of this work is to improve our understanding of the wake recovery structure of a TST to build on the limited field and laboratory data currently available in order better predict the impact of TSTs on flow and sediment transport. Detailed measurements of the wake flow structures generated by scaled TST devices are presented. These results are the first to be derived from the application of high spatial resolution stereoscopic Particle Image Velocimetry (PIV). Two scale model horizontal-axis TSTs were manufactured and deployed in a laboratory flume (11m long, 1.6m wide and 0.6m deep) at different flow speeds and heights above the bed. The results demonstrate greater wake recovery lengths for the rotor design with wider blade tips, despite the higher wake turbulence generated by the blades. Wake recovery is more rapid at the

higher flow speed when greater turbulence from the tips is observed, but wake recovery lengths increase when both rotors are positioned closer to the bed.

Keywords: Renewable, Power, Tidal, Turbine, Flow, Wake

1 INTRODUCTION

Horizontal-axis TSTs can harness energy from a current stream without the requirement to either channelize or impound the flow stream (Khan et al., 2009). TSTs generate more power than equivalent-sized wind turbines due to the higher density of water compared with air but consequently, there are greater structural stresses placed on the turbine rotor and supporting structures (Bahaj et al., 2007). Another advantage that makes tidal stream devices desirable as a renewable energy source is the repeatability and predictability of the power generation of bi-directional TSTs that are able to harness both ebb and flood currents (Charlier, 2003). Tidal power generation has the potential to become a major source of renewable energy, particularly in the UK (Burrows et al., 2009). However, take-up of the technology remains slow, due partly to concerns about adverse environmental impacts on the sea-bed ecosystem (e.g. Cada et al., 2007, Couch and Bryden, 2007).

TST wakes are characterised by a reduction in flow velocity downstream of the rotor and accelerated flow around the rotor (McCombes et al., 2011). For an array of TSTs, the wake effects of the upstream turbines affect the inflow conditions for downstream turbines causing a potential decrease in kinetic energy available to the rotor and an increase in unsteady flow velocity fluctuations. Turbulence generated at the rotor blade tips increases the bed shear stress downstream of the TST (Jordan et al., 2015) with potential adverse impacts on sediment transport and scour in the vicinity of the downstream TST supports. A good understanding of the wake development is therefore necessary to determine the optimal distance between TST devices in an array. Wake widths expand with distance downstream of the turbine but may become constrained by the water surface, altering the wake structure when compared with unconstrained flows (Myers et al., 2008). The lateral spacing of TST devices is also an important consideration as the wake recovery length has been shown to decrease as a result of the increased mixing caused by higher turbulence generated between the two adjacent TST wake structures (Stallard et al., 2013). Physical modelling of TSTs has previously focused on wake characterisation and the influence of turbulence on generating performance (e.g. Maganga et al., 2010) and, more recently, on scour development (Hill et al., 2014). Measurement of flow in laboratory flumes has tended to focus on the central vertical plane of a single rotor design using Acoustic Doppler Velocimeters (ADV) to obtain point measurements of flow across planes intersecting the TST wake (e.g., Chamorro et al. (2013), Maganga et al., (2010)). More recently, Simmons et al. (2015) demonstrated the importance of the rotor design on the generation of vortices at the blade tips and the influence of those vortices in the development of turbulent flow structures

several rotor diameters downstream of the TST using Particle Image Velocimetry (PIV). Similarly, Jordan et al. (2015) reported on the wake asymmetry that arose from the deployment of one design of rotor positioned close to a roughened bed using PIV.

This study utilises a PIV system to measure flow velocity vectors in high resolution within 2D vertical interrogation areas at different positions across the channel. This enables an improved characterisation of the turbulent wake structure downstream of the TST rotor and the recovery of the structure through interaction with the surrounding flow. Results are presented from an examination of factors thought to affect wake recovery downstream of the rotor including comparisons between two different rotor designs, two different rotor heights above the bed within the turbulent boundary layer and two different inlet flow speeds. A discussion of the effect of these factors on the wake structure is presented that focusses on differences in mixing related to the structure and magnitude of turbulent kinetic energy in the downstream wake.

2 EXPERIMENTAL SETUP

Experiments to quantify the impact on flow structure of two contrasting model rotors were conducted at the Total Environment Simulator (TES) at the University of Hull. The TES is a re-circulating flume and a working channel of 1.6 m width was constructed using partition walls to give a working section of 11 m length with a water depth of 0.6 m. The channel width minimised the side-wall effect and enabled the PIV camera housing to be mounted on a traverse in a separate section of still water outside the experimental channel. The bed of the channel was constructed from varnished, plywood boards and the flow depth ensured that the 0.2 m diameter rotors were sufficiently separated from flow surface effects (Stallard et al., 2013). Two flow regimes were used in the experiments with depth-averaged streamwise flow speeds of 0.26 ms^{-1} and 0.50 ms^{-1}. These are referred to herein as low flow and high flow respectively. The high flow regime flow rate was chosen as it was the highest flow rate at which the rotational speed of the motor, used to control the speed of the rotor, could be kept constant.

Two different rotor models were designed at the University of Strathclyde for the experiments and are shown in Fig. 1. Both horizontal-axis three-bladed rotors have a diameter of 200 mm. Rotor A has a twist of 17.6^o and 5^o fixed blade pitch, NACA 63-415 aerofoil and a tip thickness to blade radius ratio of 0.05. The blade design for Rotor B is based on that described by Vybulkova et al. (2015). It has a blade twist of 18.58^o from root to tip (including blade pitch angle that was fixed), aerofoil NACA 0012 aerofoil and a tip thickness to blade ratio of 0.141. The rotor designs are available as stereolithography (STL) files in the supplemental material. Both rotors have comparable power coefficients but different aerofoil and blade-tip shapes to provide a comparison between the impact of narrow-bladed and wide-bladed rotors on flow structure. In practice, TSTs are likely to be designed with wider blade tips than similar horizontal-axis wind-turbine rotors in order to provide structural strength to withstand the greater forces placed on them

(Fraenkel, 2010). The model rotors used in the flume were manufactured from these designs using stereo-lithography and were mounted on an 8 mm diameter shaft attached to a motor through a watertight seal and flexible coupling. The rotor speed was controlled by the 25W DC motor that enabled the tip-speed ratio of the rotor to be set and controlled remotely. The motor was chosen to provide sufficient stability and power to control the rotor at a tip-speed ratio of 5.5, chosen to represent the maximum of the power curve, for the low flow regime (137 RPM) and high flow regime (263 RPM) but with a small diameter to minimise the impact of the motor housing on the flow. The motor housing and support were designed as a solid piece with a 32mm diameter housing attached to a 68 mm x 6 mm solid fin that enabled the rotor to be supported from above and positioned at different heights above the channel bed. The rotor was supported from above to enable quantification of the rotor's impact on flow without the impediment of a bed-mounted support. The rotor was positioned ~6.5 m from the inlet to allow the flow to become fully developed before encountering the rotor. Fig. 2(a) shows Rotor B attached to the housing from a position upstream in the channel looking towards the channel outlet. The power and control cables exit the housing through a seal at the downstream end of the housing.

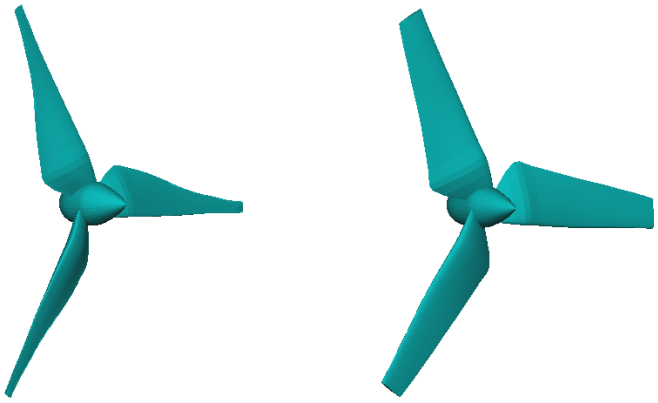

(a) **(b)**

Fig. 1. CAD images of the two rotor designs: (a) Rotor A and (b) Rotor B

Images of the laser-illuminated, seeded flow downstream of the rotor were captured with two submersed cameras that formed a stereoscopic, dual-pulse laser PIV system. The system thus enabled the derivation of 3-component velocity vectors across a 2D interrogation area aligned with the streamwise axis. The laser was positioned downstream of the rotor on a frame mounted above the channel. The laser beam was directed through an optic, positioned approximately 0.2 m above the channel bed at around 2 m downstream of the rotor, which created a vertical, light-sheet orientated parallel to the channel centreline. The intersection of the light-sheet with the channel bed and the cylindrical camera housing is seen in Fig. 2(b) before the tank was filled with water. The laser-mounting and the camera housing traverse allowed the light-sheet to be re-positioned at different locations across the channel whilst maintaining the geometrical arrangement between the light-sheet and the two cameras, which captured images through the clear, Perspex walls from positions downstream and upstream of the interrogation area. The traverse also allowed

the camera housing to be moved to different positions in the streamwise and vertical axes. Image pairs of 2320 pixels by 1726 pixels were captured with an interval of 3000 µs on two digital cameras at a repetition frequency of 30 Hz covering a field of view of approximately 440 mm x 310 mm. A 3D calibration was obtained for the system using a multi-level target positioned on the centreline of the channel. During experiments, the flow was carefully seeded with a concentration of particles that enabled high resolution PIV processing without attenuating the light-sheet due to particle scattering. The seeding material used throughout the experiments was a copolymer coating powder with a quoted size range of 95% less than 180µm. Fig. 3(a) shows the seeding material illuminated by the light-sheet during acquisition. Fig. 3(b) shows a typical PIV camera image of the seeded flow with Rotor B in operation. The motor housing and channel bed are illuminated on the centreline by the light-sheet and the control and communications cable can be seen exiting the rear of the motor housing.

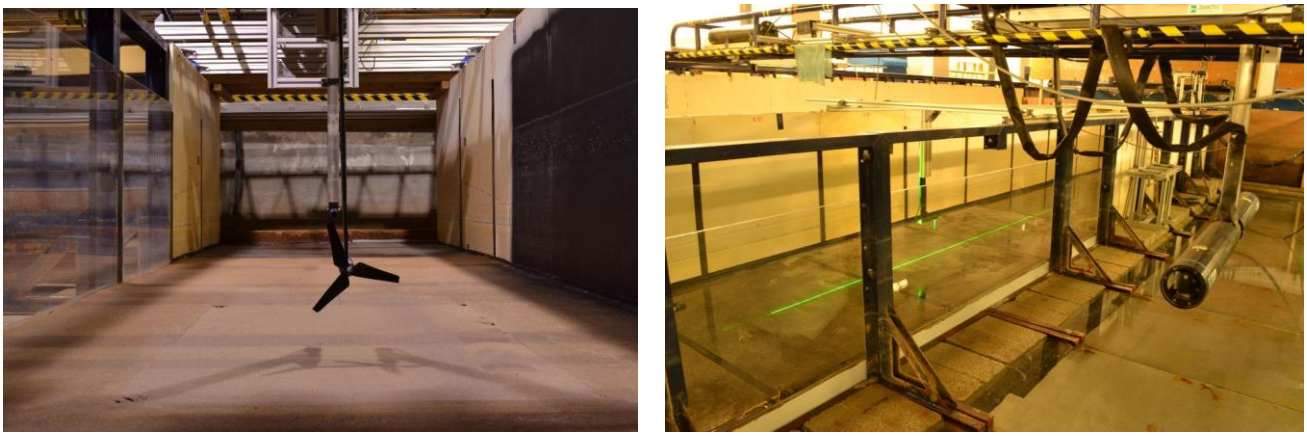

(a) **(b)**

Fig. 2. (a) Looking downstream towards Rotor B positioned at the centre of the channel and (b) the PIV camera housing mounted below the traverse (right-hand side of image) looking through the Perspex channel side-wall prior to filling with water

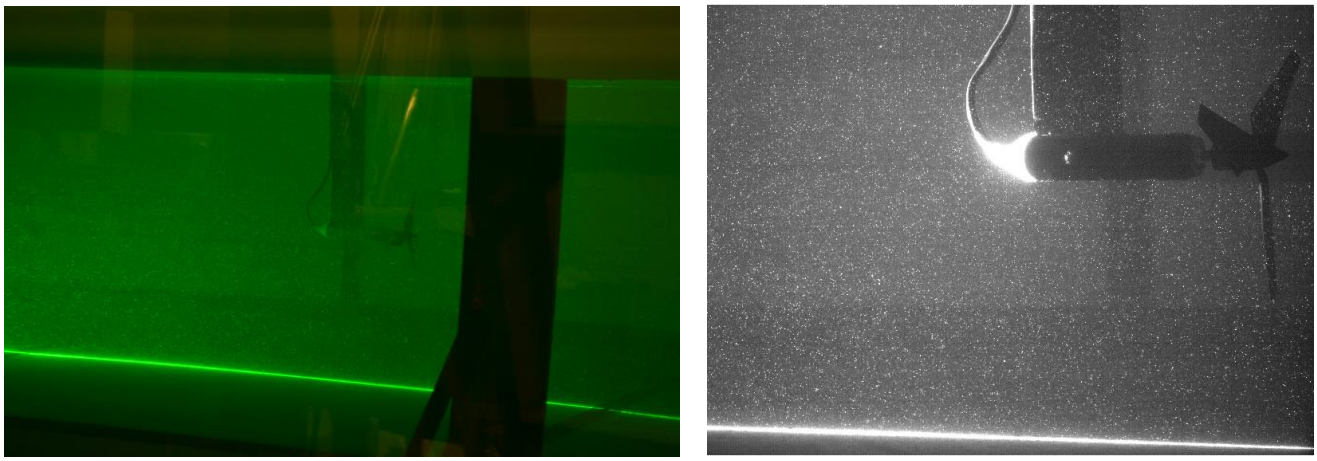

(a) **(b)**

Fig. 3. (a) Particles illuminated by the laser light-sheet at position $y = 0$ and (b) single PIV camera image

The schematic diagram in Fig. 4 shows a cross-section of the channel and the coordinate system used herein, with *x* representing the streamwise direction towards the outlet, y representing the across-stream

direction from true left-hand side to true right-hand side and *z* the vertical direction upwards. Positions are described relative to the origin at the rotor cone tip. The positions of the interrogation areas in relation to the rotor and light-sheet optic are shown down-stream of the rotor. Images were acquired with the camera housing positioned at three streamwise positions downstream of the rotor cone tip, centred at x = 196 mm, x = 341 mm and x = 586 mm and at three vertical positions centred at z = -49 mm, z = 116 mm and z = 281 mm relative to a rotor cone tip positioned at 200 mm above the bed. The six lower positions shown in Fig. 4 represent the full interrogation domain for the rotor experiments, covering an area of approximately three quarters of the flow depth above the bed and a length of 930 mm in the *x*-axis. The three positions in the vertical from the bed to the flow surface at the upstream location of z = -49 mm coincident with the rotor mounting were used to determine the baseline measurements of the flow in the plain channel without the rotor and support.

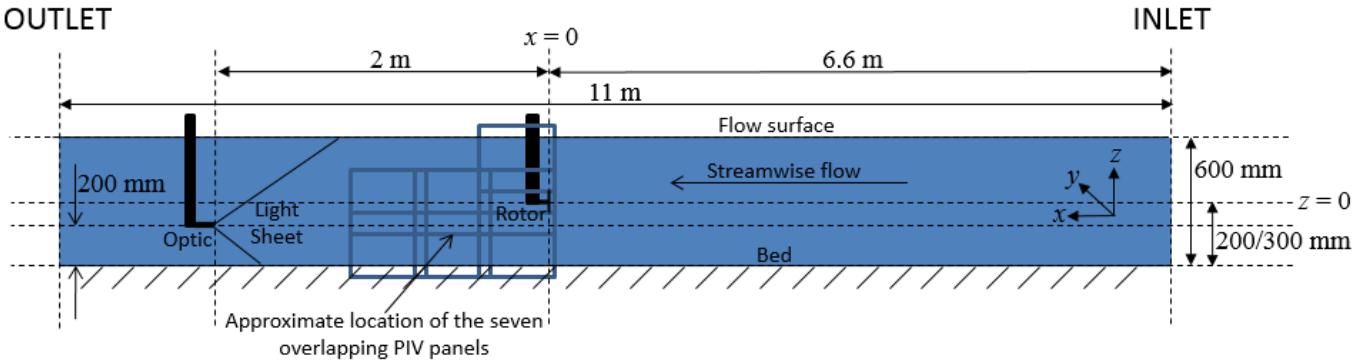

Fig. 4 Flume cross section showing the positions of the seven PIV interrogation areas in relation to the rotor and light-sheet optic

Sets of 3600 image pairs were acquired at each location over a period of 120 s which was sufficient to capture the mean flow statistics. Image sets were collected at intervals of 30 minutes to allow for data acquired to RAM to be transferred to storage disks. The acquired PIV images were processed using Dantec Dynamic's capture and processing software, Dynamic Studio. The results presented herein were obtained using the 'Adaptive PIV' algorithm (Theunissen et al., 2007), which iteratively adjusts the size and shape of the image interrogation window on the basis of local seeding density and velocity gradient. Baseline profiles for the plain channel without the rotor and support, were obtained with a grid spacing of 16 x 16 pixels, a minimum interrogation area of 32 x 32 pixels and a maximum interrogation area of 64 x 64 pixels.

3 RESULTS

Fig. 5 shows the mean values of the streamwise, *u*, across-stream, *v*, and vertical, *w*, components of the velocity vectors obtained by averaging the velocity vector components between the *x*-axis limits of 125 mm and 384 mm downstream of where the rotor cone tip would be positioned at ~200 mm above the bed

(x = 0, y = 0, z = 0). Fig. 5(a) and (b) show the respective mean profiles for the low flow and high flow regimes. Similar patterns in the mean components of velocity, $\bar{u}$, $\bar{v}$, and $\bar{w}$, are observed for both flow regimes: $\bar{u}$ increases as expected from the boundary at the channel bed to z = ~100 mm, however there is a marginal decrease in mean flow speed higher in the water column with a local minimum below the flow surface at around 400 mm above the origin. This effect is likely to be caused by secondary currents that characterize flow in channels with low width to depth ratios (e.g. Nezu and Nakagawa., 1993). The mean of the vertical component, $\bar{v}$, is close to zero throughout the water column but a small across-stream circulation is shown in the values of $\bar{w}$ with a root mean square value through the full flow depth of 0.019 m s^{-1} at the low flow regime and 0.042 m s^{-1} at the high flow regime. Values of shear velocity, u_*, are derived as u_* = 0.016 m s^{-1} for the low flow regime and u_* = 0.031 m s^{-1} for the high flow regime using a regression of the lower 50 mm of the streamwise velocity and log of the normalised height above the bed, where

$$u_* = \frac{\kappa . u}{ln(Z/Z_0)} \quad (1)$$

and κ is the von Karman constant, with a value of 0.40, Z is the height above the bed, and Z_0 is the full flow depth from bed to surface.

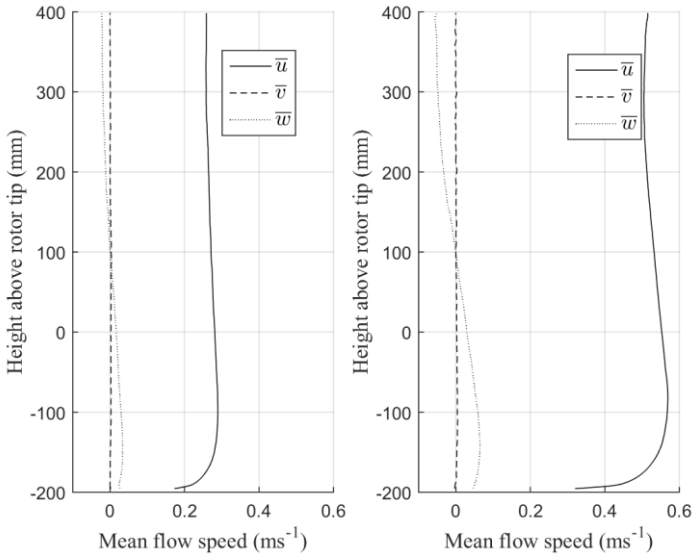

Fig. 5. Mean velocity components, $\bar{u}$, $\bar{v}$ and $\bar{w}$, for the plain channel low flow regime, (a), and high flow regime, (b)

Figs. 6-11 show flow maps derived by combining the statistics of six PIV interrogation areas for both Rotor A and Rotor B with the rotor centres positioned at 200 mm and 300 mm above the bed. The velocity statistics were derived from the results obtained by processing using adaptive PIV with a grid spacing of 32 x 32 pixels, a minimum interrogation area of 16 x 16 pixels and a maximum interrogation area of 32 x 32 pixels. The overlapping areas of the interrogation areas around the border were removed and slight differences between adjoining areas can be seen which probably result from the low frequency flow structures present in the channel. The approximate location of the rotor tip, shaft, motor housing, support and

control cable are blanked out in black for results obtained on the centreline. However, there are regions near the blanked area that may contain artefacts related to the solid objects in the image. The top right corner of the images are blanked out in white as this region, upstream of the housing and support, was not illuminated by the light-sheet.

Fig. 6 shows the normalised mean of the streamwise component of velocity, $\bar{u}/u_*$, for the high flow regime on the centreline. A wake region of decelerated mean flow can clearly be discerned downstream of the rotors. The vertical width of the decelerated wake structure is greater for Rotor B compared with Rotor A. Fig. 7 shows the equivalent plots for the data acquired at y = -100 mm. There is little change to the mean values of $\bar{u}/u_*$ for Rotor A compared with the plain channel flow without the rotor shown in Fig. 5. However, there is a marked deceleration for Rotor B. The greater vertical extent of the wake deceleration on the centreline and the deceleration at y = -100 mm for rotor B can be explained by the increased blockage to the flow related to Rotor B's wider rotor blade tips.

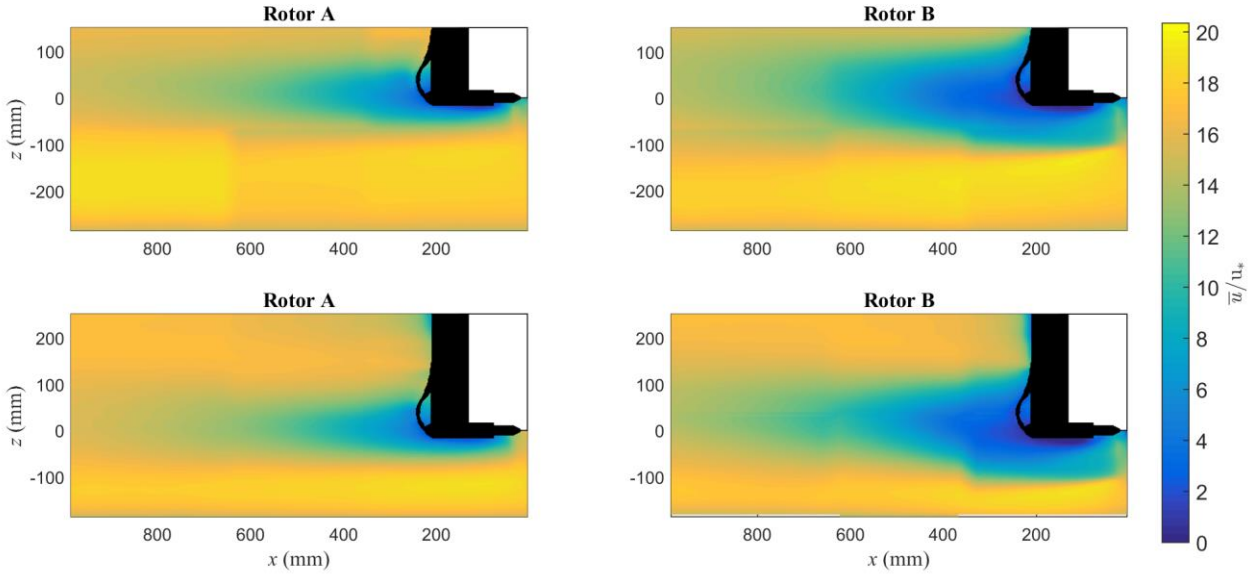

Fig. 6. Flow maps of normalised mean streamwise flow speed for Rotor A (left) and Rotor B (right) positioned at 300 mm (top) and 200 mm (bottom) above the bed for the channel centre (y = 0) at the high flow regime

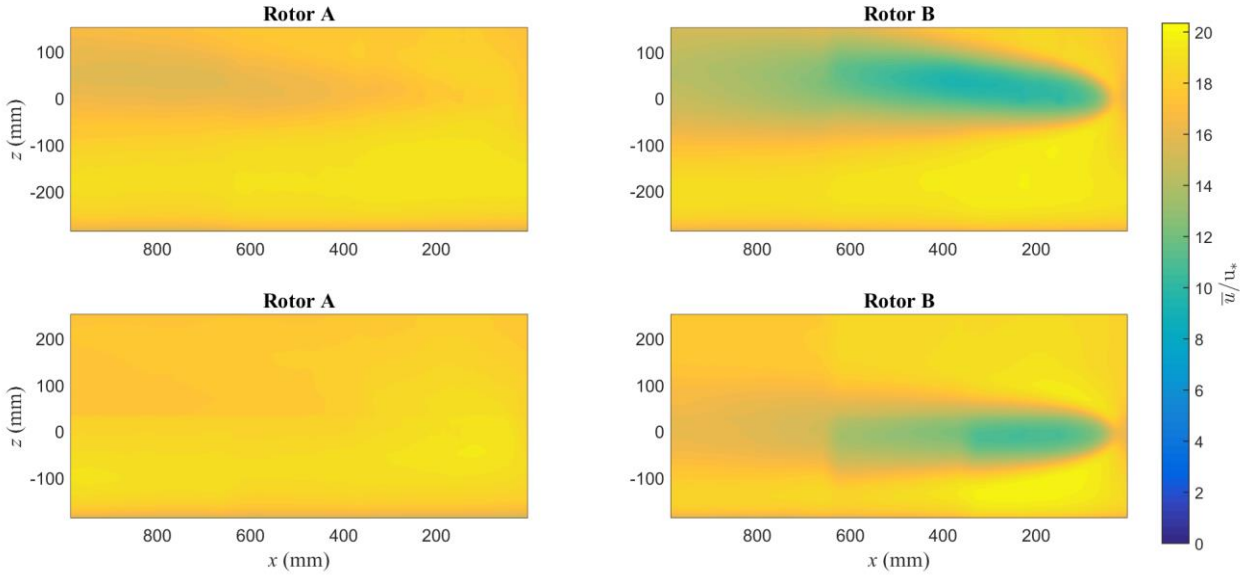

Fig. 7. Flow maps of normalised mean streamwise flow speed for Rotor A (left) and Rotor B (right) positioned at 300 mm (top) and 200 mm (bottom) above the bed at 100 mm off the channel centre on the true left-hand side (y =-100 mm) at the high flow regime

The plots in Fig. 8 show the normalised turbulent kinetic energy, k/u_*^2, for Rotor A and Rotor B and for rotor tip positions of 300 mm and 200 mm above the bed where k is defined as:

$$k = \frac{1}{2}\left(\overline{u'^2} + \overline{v'^2} + \overline{w'^2}\right) \quad (2)$$

and where u', v' and w', denote the fluctuating component of u, v, and w about their respective mean values. Two regions of higher magnitude turbulent kinetic energy, originating from the upper and lower surface of the motor housing, can be seen propagating downstream from an origin close to the centre of Rotor A and merging between x = 300 and x = 400 mm. Similar regions of higher intensity k/u_*^2 originating from the surfaces of the motor housing, can be seen for Rotor B. However, a much larger magnitude wake structure develops from two narrow regions of higher k/u_*^2 values that propagate from the location of the rotor blade tips of Rotor B at x = 0 mm, y = 0 mm, z = ±100 mm and which then merge to form a single region of high intensity between 400 mm and 600 mm downstream of the rotor. At y = -100 mm, for Rotor A (Fig. 9), there is a marginal increase in k/u_*^2 downstream from around x = 400 mm centred on the z = 0 mm axis but there is a much more marked increase in the magnitude of k/u_*^2 in the wake of Rotor B. Two narrow regions originating from a position coincident with the centre of the rotor in the y = -100 mm plane extend downstream and merge around x = 200 mm to x = 300 mm. The upper and lower boundaries of the high intensity region grow in vertical extent with distance downstream with the highest magnitudes around the vertical centre of the wake between approximately x = 300 mm to x = 700 mm. The results show the greater vorticity generated by the wider tips of Rotor B.

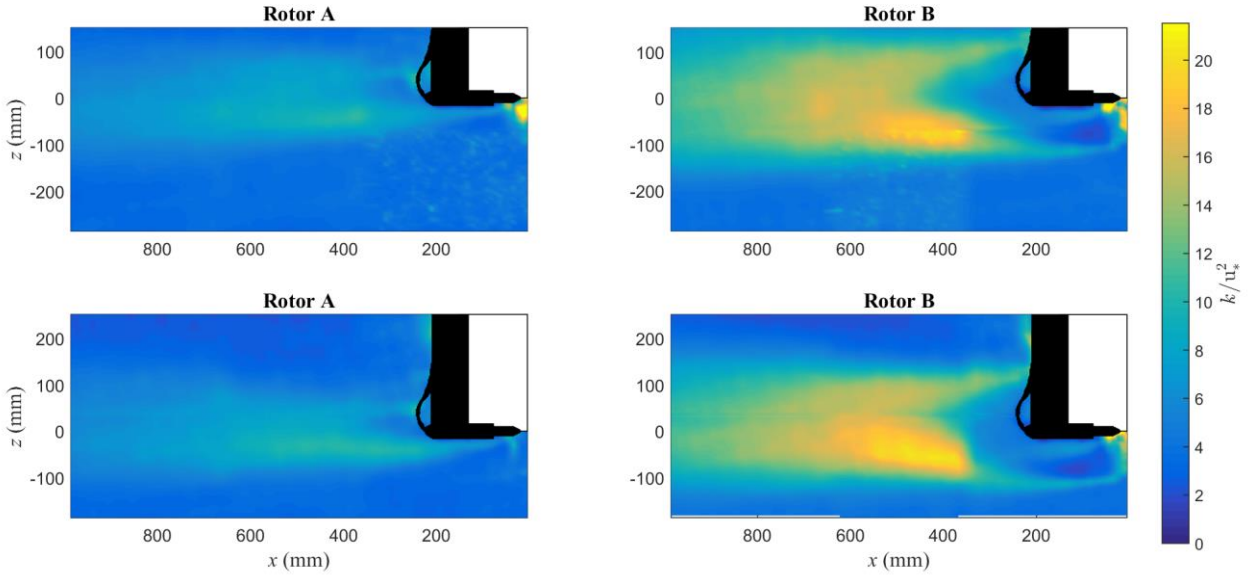

Fig. 8. Flow maps of normalised turbulent kinetic energy for Rotor A (left) and Rotor B (right) positioned at 300 mm (top) and 200 mm (bottom) above the bed for the channel centre (y = 0) at the high flow regime

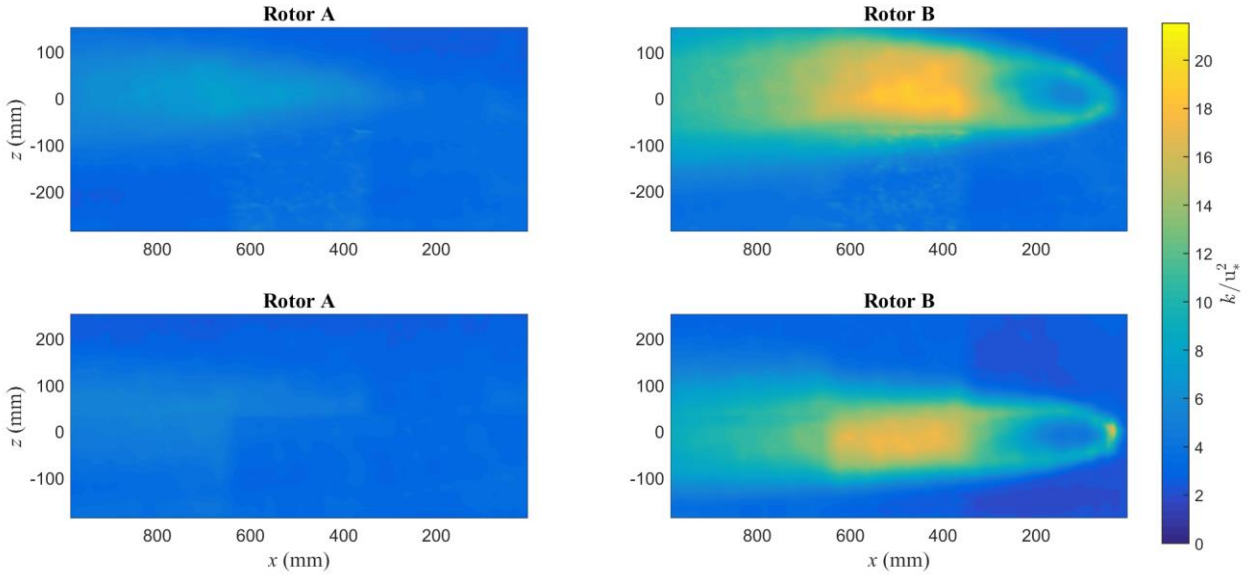

Fig. 9. Flow maps of normalised turbulent kinetic energy for Rotor A (left) and Rotor B (right) positioned at 300 mm (top) and 200 mm (bottom) above the bed at 100 mm off the channel centre on the true left-hand side (y =-100 mm) at the high flow regime

Fig. 10 shows the flow maps of the normalised mean streamwise velocity, $\bar{u}/u_*$, and Fig. 11 shows the flow maps of the normalised turbulent kinetic energy, k/u_*^2, at the low flow regime. The wake structures in Fig. 10 can be seen to extend further downstream compared with the equivalent plots for the high flow regime shown in Fig. 6. Lower magnitude values of k/u_*^2 can be seen in the wake at around x = 300 mm to x = 700 mm at the lower flow regime in Fig. 11 compared with the same four scenarios presented in Fig. 8 at the high flow regime.

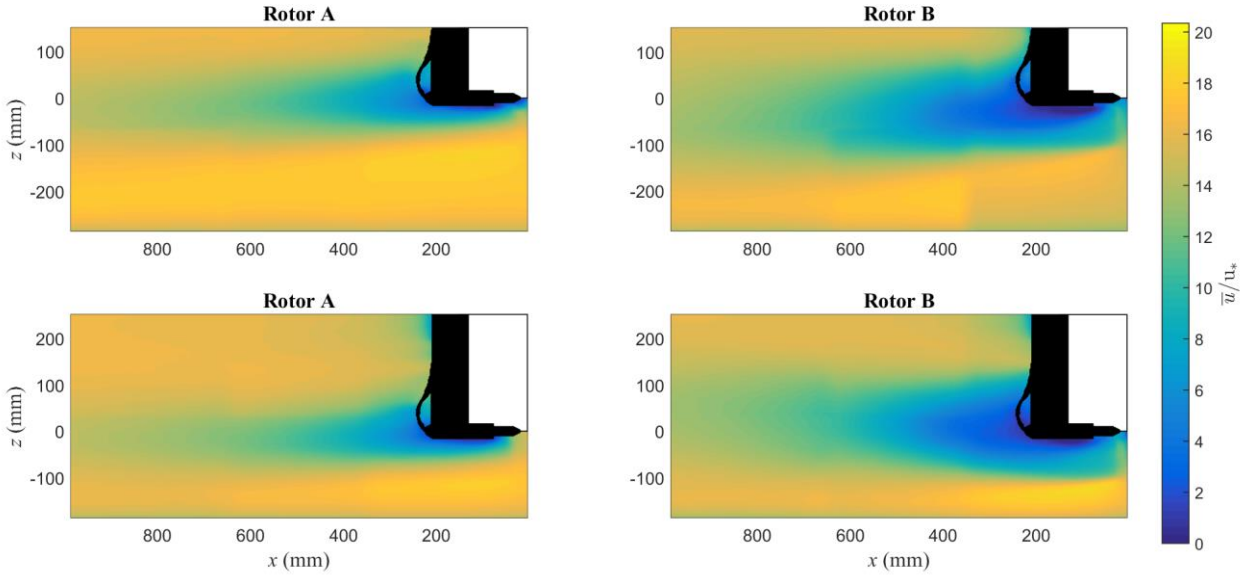

Fig. 10. Flow maps of normalised mean streamwise flow speed for Rotor A (left) and Rotor B (right) positioned at 300 mm (top) and 200 mm (bottom) above the bed for the channel centre (y = 0) at the low flow regime

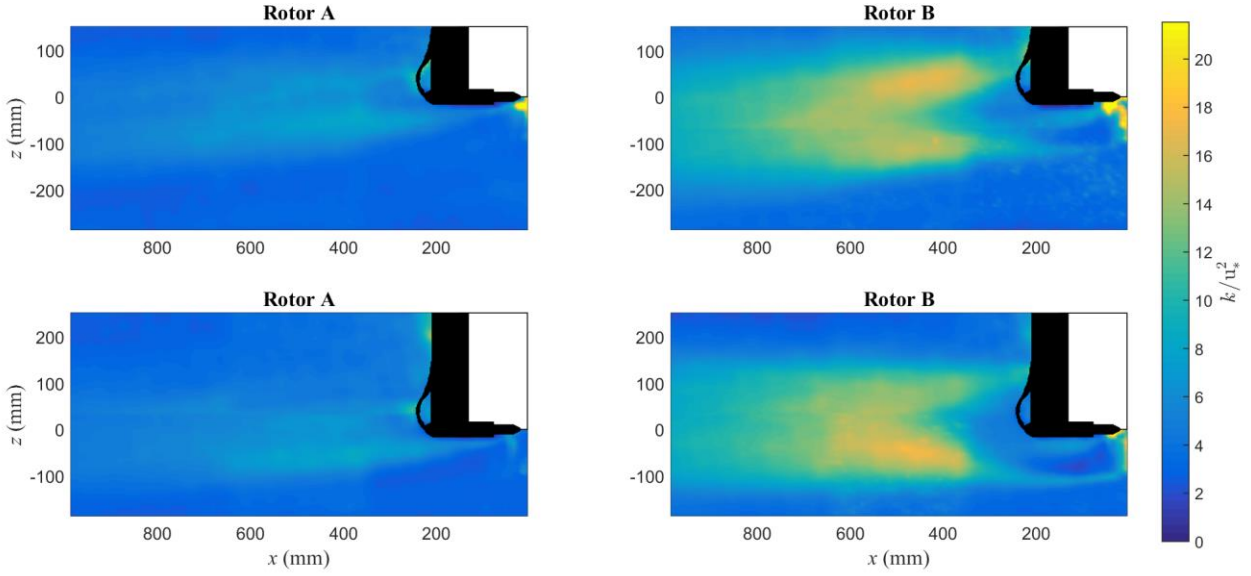

Fig. 11. Flow maps of normalised turbulent kinetic energy for Rotor A (left) and Rotor B (right) positioned at 300 mm (top) and 200 mm (bottom) above the bed for the channel centre (y = 0) at the low flow regime

To assess the development of the wake recovery with distance downstream from the rotor, the mean streamwise component of flow is expressed as a percentage of the mean streamwise profile through the water column that was measured for the plain channel without the rotor and support present for both flow regimes, as shown in Fig. 5. Fig. 12 demonstrates an example of the wake structure expressed in these terms for one of the scenarios, with Rotor A positioned 300 mm above the bed at the low flow regime. The vertical width of the wake is evaluated downstream of x = 230 mm, denoted by the vertical line, as velocity vectors in the region closer to the rotor are reasoned to be influenced by the image of the rotor support. The contour lines denote where the mean streamwise flow velocity is 85%, 75% and 50% of the plain channel values at the same height above the bed. The vertical width of the wake is defined as the vertical distance between the same contour line, as shown in the plot. The vertical width is thus evaluated

for the eight different experimental scenarios involving Rotor A and Rotor B at both flow regimes and with the rotor cone tip positioned at 200 mm and 300 mm above the bed. Fig. 13 shows the development of the vertical width for the eight scenarios for widths defined as (a) 85%, (b) 75% and (c) 50% of the mean streamwise flow velocity.

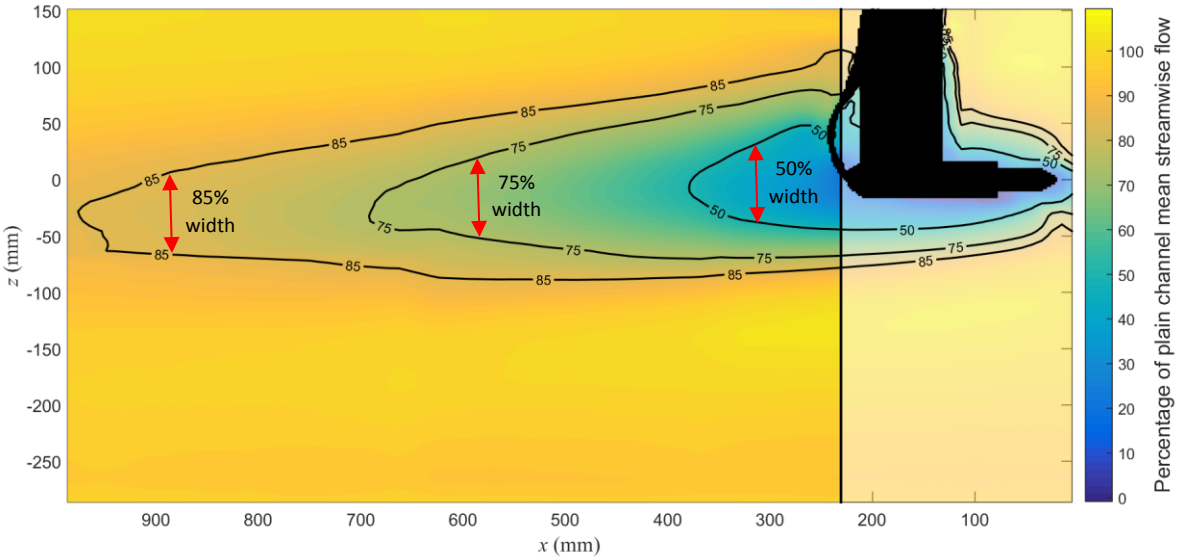

Fig. 12 Mean streamwise flow as a percentage of the mean vertical profile of the plain channel flow for Rotor A positioned 300 mm above the bed at the low flow regime. The vertical wake widths are defined by the contours at 50%, 75% and 85%

For three of the scenarios, all involving Rotor A, the wake velocity recovers to exceed 85% of the mean plain channel flow velocity within the measurement area, as shown in Fig. 13(a). At the other extreme, the vertical width is still between ~75 and ~200 mm at the farthest measurement location downstream at x = 986 mm for all four scenarios involving Rotor B, which all have slower wake recovery throughout the extent of the downstream measurement range compared with the same flow regimes and positions above the bed for Rotor A. The wake remains larger in vertical extent at the end of the measurement area (x = 986 mm) in all cases where the rotor positioned at 200 mm above the bed compared with the rotor at 300 mm above the bed, suggesting that wake recovery is slower when the rotor mounted closer to the bed surface. The wake width is also reduced at the farthest extent downstream or has fully recovered more rapidly for all scenarios at the high flow regime compared with the low flow regime. Fig. 13(b) shows that the wake velocity has fully recovered to 75% of the mean plain channel flow velocity within the measurement area. The wake velocity exceeds 75% of the mean plain channel flow velocity for all four Rotor A scenarios between x = ~630 mm and x =~730 mm. This contrasts sharply with Rotor B, for which the mean streamwise flow velocity recovers to exceed 75% of the mean plain channel flow velocity between x = ~800 mm and x = ~900mm. For all scenarios, recovery to greater than 75% occurs at a greater distance downstream with the rotor positioned at 200 mm above the bed compared with 300 mm above the bed. Except for Rotor B at 300 mm above the bed, the distance downstream to full recovery above 75% of the mean flow velocity occurs at a greater distance downstream for the low flow regime

than for all other scenarios. For recovery to greater than 50% of the mean plain channel streamwise flow velcoity, shown in Fig. 13(c), the difference in recovery distance downstream of the rotor cone tip is noticeably different for Rotor A at x = ~400 mm and Rotor B at x = ~440 mm to x = ~450 mm. Differences in full recovery distance to greater than 50% are difficult to discern for comparisons between flow regimes and rotor position.

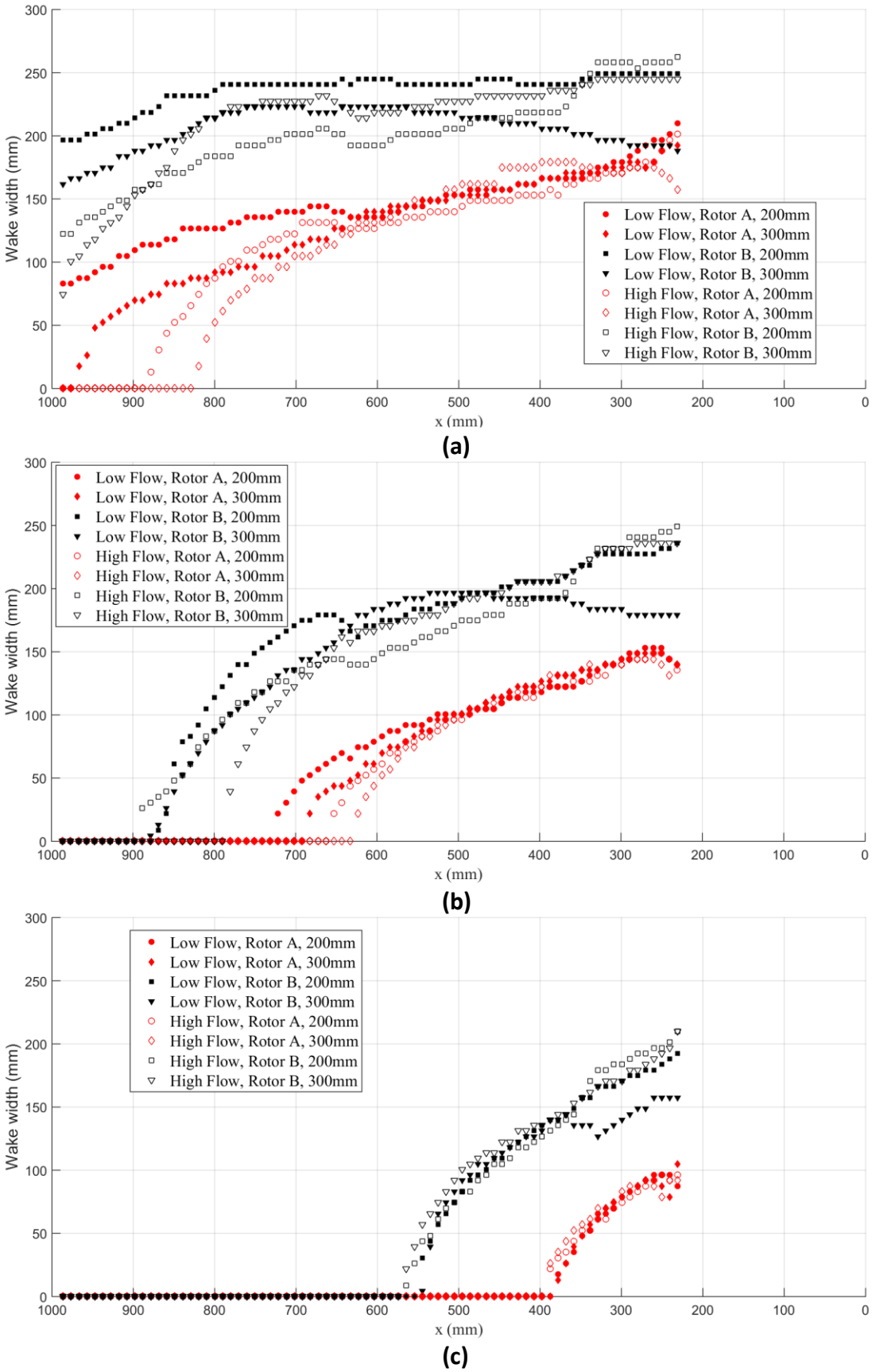

Fig. 13. Wake width downstream of the rotor calculated using a threshold of (a) 85%, (b) 75% and (c) 50% of plain channel mean streamwise flow

4 DISCUSSION

The slower wake recovery of the high flow regime scenarios compared with the low flow regime scenarios shown in Fig. 13 appear to be related to reduced mixing efficiency related to the lower magnitude values of k/u_*^2within the wake flow-structure which can be seen in the differences of the flow maps in Fig. 11 compared with Fig. 8. However, the much higher values of k/u_*^2 observed with rotor B compared with Rotor A for all four scenarios in Fig. 8 and Fig. 11 do result in greater wake recovery lengths in Fig. 13 rather than shorter recovery lengths. This is probably due to the greater mixing required break-down the initially wider wake structure that develops immediately downstream from Rotor B (Fig. 6 and Fig. 10) resulting from Rotor B's greater relative flow blockage due to the wider rotor tips. Myers and Bahaj (2010) report greater recovery lengths for a porous actuator disk when positioned closer to the bed but without an increase in turbulent kinetic energy in the wake or between the bed and the lower boundary of the wake. Similarly, Jordan et al. (2015) report results that compares the wake of Rotor B, as described herein, over a roughened, flat bed with the rotor cone tip position 200 mm and 120 mm above the bed. There is a marked decrease in turbulent kinetic energy in the lower half of the wake with the rotor positioned at 120 mm above the bed compared with 200 mm above the bed, but an increase in the wake recovery length. The increase in wake recovery lengths at 200 mm compared with 300 mm shown in Fig. 13 agrees, therefore, with previous observations of increased recovery lengths as the rotor is positioned closer to the bed. There are noticeable changes to the distribution of normalised turbulent kinetic energy in the vertical between the two rotor positions. Profiles of k/u_*^2 as a function of *z* are shown in Fig. 14 for two locations downstream of the rotor. When the rotor is positioned at 300 mm above the bed, the profiles are noticeably asymmetric for the larger wake of Rotor B at both x = 500 mm and x = 800 mm downstream of the rotor. There is greater turbulent energy for both low and high flow regimes between the bed and z = -50 mm to -100 mm when Rotor B is positioned at 300 mm compared with the same near-bed region when the rotor is positioned at 200 mm above the bed. The reduction in near-bed turbulent kinetic energy agrees with the larger asymmetry observed by Jordan et al. (2015) with the same rotor positioned at 120 mm above the bed and suggests that less efficient mixing in the near-bed region is extending the wake recovery length.

Factors that affect wake recovery lengths are important considerations in the layout design of TST arrays. A longer wake recovery distance will necessitate greater streamwise distances between TST devices in a rectilinear grid array to minimise the impacts of velocity deficits and unsteady fluctuations on TST efficiency, and also the transport and scour of bed sediment around turbine support structures. Conversely, staggered grid arrays (see Turnock et al., 2011) may benefit from the accelerated flows surrounding the wake that will persist with greater wake recovery lengths.

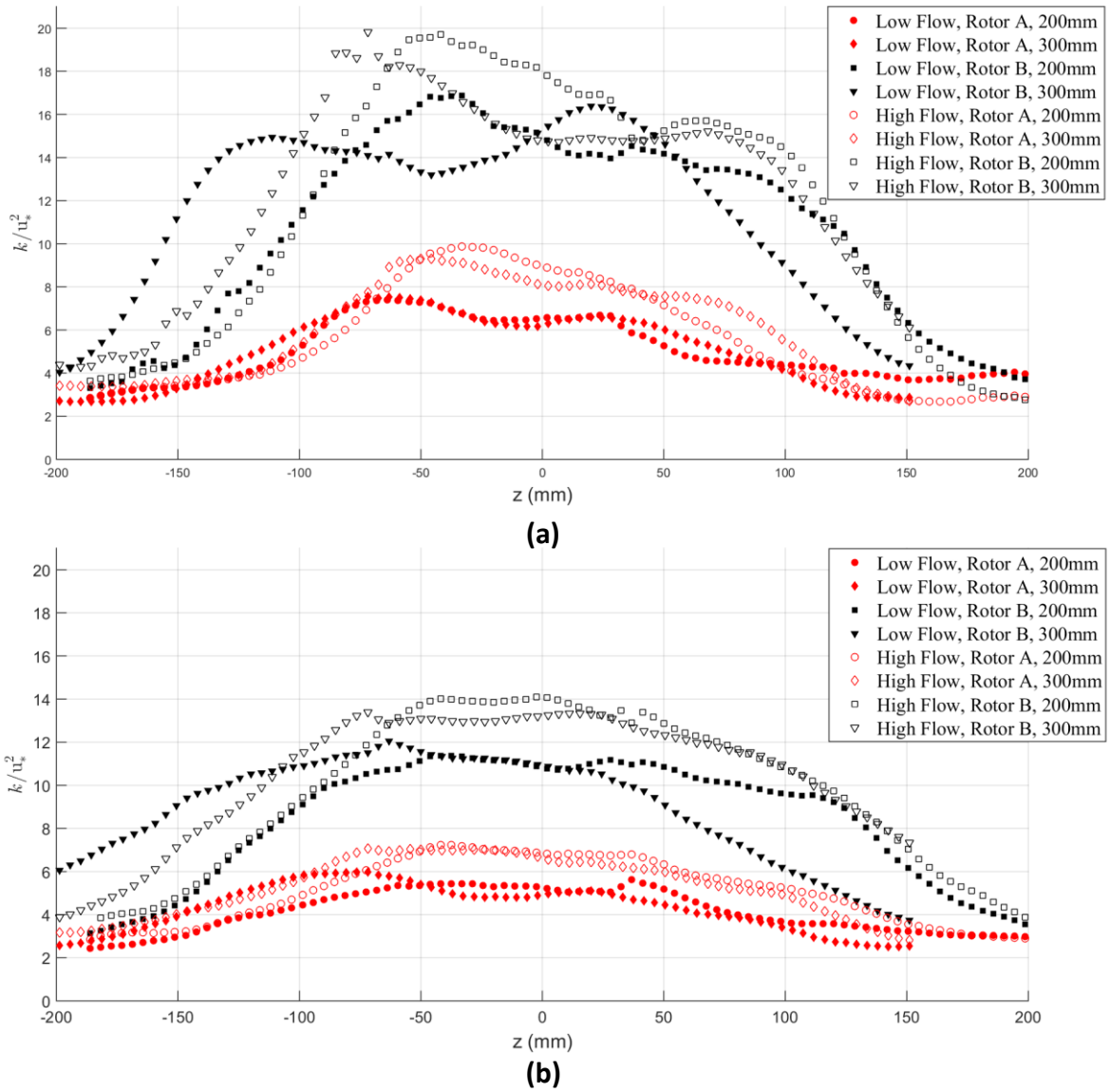

Fig.. 14 Profiles of normalised turbulent kinetic energy as a function of vertical distance relative to the rotor cone tip at (a) x = 500 mm and (b) x = 800 mm downstream of the rotor

5 CONCLUSIONS

Detailed flow maps have been presented of the normalised mean streamwise flow and turbulent kinetic energy of the wakes downstream of two designs of TST rotor. The effects on wake recovery of factors including rotor design, rotor height above the bed and flow speed have been examined. The broad-tipped Rotor B generates significant vortex shedding from the blade tips that converge to form a region of high energy turbulence in the centre of the wake. In comparison, Rotor A produces a narrower wake with a region of comparatively lower magnitude turbulence originating from the motor housing without significant vortex shedding from the blade tips. Wake recovery lengths for Rotor B are greater than for Rotor A despite the increased turbulence in the wake. This is reasoned to be caused by the increased flow deceleration related to the larger blockage to flow of the rotor's wider blade tips. Recovery lengths are shorter for the high flow regime where there is a region of larger magnitude turbulence in the wake compared with

the low flow regime. The higher magnitude turbulence is assumed to cause more efficient mixing of the wake and surrounding fluid. Recovery lengths are also observed to increase when both rotors are positioned lower in the flow and these results agree with the results of other physical model results for rotors and actuator disks within the boundary layer.

ACKNOWLEDGEMENT

This work was funded by the Engineering and Physical Science Research Council (EPSRC) [grant reference number: EP/J010359/1]. The designs for the two rotors were provided by project partners at the University of Strathclyde.

REFERENCES

Bahaj, A.S., Molland, A.F., Chaplin, J.R., Batten W.M.J., (2007) Power and thrust measurements of marine current turbines under various hydrodynamic flow conditions in a cavitation tunnel and a towing tank, Renewable Energy, 32(3), pp. 407-426

Burrows, R., Yates, N.C., Hedges, T.S., Li, M., Zhou, J.G., Chen, D.Y., Walkington, I.A., Wolf, J., and Procter, R. (2009). Tidal enery potential in UK waters. Proceedings of the ICE - Maritime Engineering, 162, pp. 155-164

Cada, G., Ahlgrimm, J., Bahleda, M., Bigford, T., Stavrakas, S..D., Hall, D., Moursund, R., Sale, M. (2007). Potential impacts of hydrokinetic and wave energy conversion technologies on aquatic environments. Fisheries, 32(4), pp. 174–181.

Chamorro, L. P., Hill, C., Morton, S., Ellis, C., Arndt, R. E. A., Sotiropoulos, F. (2013). On the interaction between a turbulent open channel flow and an axial-flow turbine. J. Fluid Mech., 716, pp. 658–670.

Charlier, R.H., (2003). A "sleeper" awakes: tidal current power. Renew. Sustain. Energy Rev. 7(3), pp. 187-213

Couch, S.J., Bryden, I.G. (2007) Large-scale physical response of the tidal system to energy extraction and its significance for informing environmental and ecological impact assessment. Proceedings, Oceans 2007 - European International Conference, pp. 912-916

Fraenkel, P. (2010). Practical tidal turbine design considerations: a review of technical alternatives and key design decisions leading to the development of the SeaGen 1.2MW tidal turbine, Proceedings - Fluid Machinery Group - Ocean Power Fluid Machinery Seminar, Institute of Mechanical Engineers, London, pp. 1-19

Hill, C., Musa, M., Chamorro, L., Ellis, C., Guala, M.(2014). Local Scour around a Model Hydrokinetic Turbine in an Erodible Channel. Journal of Hydraulic Engineering, 140(8), (doi: 10.1061/(ASCE)HY.1943-7900.0000900, 04014037)

Jordan, L. B., Simmons, S., McLelland, S., Murphy, B., Parsons, D. and Vybulkova, L., (2015). The impact of tidal stream turbines on 3D flow and bed shear stress measured with particle image velocimetry in a laboratory flume. In: Proceedings of the 11th European Wave and Tidal Energy Conference (EWTEC). Nantes, France, Sept. 2015

Khan, , M.J., Bhuyan, G., Iqbal, M.T., and Quaicoe, J.E. (2009). Hydrokinetic energy conversion systems and assessment of horizontal and vertical axis turbines for river and tidal applications: a technology status review. Appl. Energy **86**, pp.1823-1835

Maganga, F., Germain, G., King, J., Pinon, G., Rivoalen, E. (2010). Experimental characterization of flow effects on marine current turbine behavior and on its wake properties. Ren. Power Gen. IET, 4(6), pp. 498–509.

McCombes, T., Johnstone, C., and Grant, A. (2011). Unsteady wake modelling for marine current turbines, IET Renewable Power Generation, **5**, pp. 299-310

Myers, L.E., Bahaj, A.S., Rawlinson-Smith, R.I., Thomson, M. (2008). The effect of boundary proximity upon the wake structure of horizontal axis marine current turbines. Proc. ASME 27th Conf., Portugal. OMAE2008-57667

Myers, L. E. and Bahaj, A. S. (2010) Experimental analysis of the flow field around horizontal axis tidal turbines by use of scale mesh disk rotor simulators. Ocean Engineering, 37, (2-3), 218-227. (doi:10.1016/j.oceaneng.2009.11.004).

Nezu, I., Nakagawa, H., (1993). Turbulence in Open Channel Flows, IAHR Monographs, Taylor and Francis

Simmons, S.M., McLelland, S.J., Parsons, D.R, Murphy, B.J., Jordan, L.B. & Vybulkova, L., "Flume measurements of the wake of two model horizontal-axis tidal stream turbines." (2015), Proceedings of the 2nd International Workshop on Hydraulic Structures: Data validation, Coimbra, Portugal.

Stallard, T., Collings, R., Feng, T., & Whelan, J. (2013). Interactions between tidal turbine wakes: experimental study of a group of three-bladed rotors. Phil. Trans. R. Soc. A, 371(1985), 20120159

Theunissen, R., F. Scarano, and M. L. Riethmuller. (2007), An adaptive sampling and windowing interrogation method in PIV. Measurement Science and Technology 18.1, pp. 275-287.

Turnock, S.R., Phillips, A.B., Banks, J., and Nicholls-Lee, R. (2011), Modelling tidal current turbine wakes using a coupled RANS-BEMT approach as a tool for analysing power capture of arrays of turbines. Ocean. Eng., 38 (2011), pp. 1300–1307 http://dx.doi.org/10.1016/j.oceaneng.2011.05.018

Vybulkova, L., Vezza, M. and Brown, R. (2015). "Simulating the Wake Down-stream of a Horizontal-axis Tidal Turbine Using a Modified Vorticity Transport Model", IEEE Journal of Oceanic Engineering, Vol. PP, Issue 99, June 2015, pp. 1-6.